Composites Part B 281 (2024) 111519

Contents lists available at ScienceDirect

Composites Part B

journal homepage: www.elsevier.com/locate/compositesb

Development of Ag@Si composite sinter joining with ultra-high resistance to thermal shock test for SiC power device: Experiment validation and numerical simulation

Yang Liu [a], Chuantong Chen [a,*], Ye Wang [b], Zheng Zhang [a], Ran Liu [a], Minoru Ueshima [c], Ichiro Ota [c], Hiroshi Nishikawa [d], Masahiko Nishijima [a], Koji S. Nakayama [a], Katsuaki Suganuma [a]

[a] Flexible 3D System Integration Laboratory, Osaka University, 8-1, Mihogaoka, Ibaraki, Osaka, 567-0047, Japan
[b] School of Reliability and Systems Engineering, Beihang University, Beijing, 100191, China
[c] Daicel Corporation, Grand Front Osaka Tower-B, 3-1, Kita-ku, Osaka, 530-0011, Japan
[d] Joining and Welding Research Institute, Osaka University, 11-1, Mihogaoka, Ibaraki, Osaka, 567-0047, Japan

ARTICLE INFO

Handling editor: Hao Wang

Keywords:
Ag@Si composite sintering
Enhanced reliability
Closer matched CTE
Inhibited degradation
Buildup stress mitigation

ABSTRACT

Owing to its cost-effectiveness and low coefficient of thermal expansion (CTE), micron Si is incorporated into sintered Ag matrix to develop an Ag@Si composite sintering strategy. The Si integration helps reduce cost and alleviate CTE-mismatch of Ag-sintered die attachments. An innovative Ag@Si composite sintering structure is achieved by low-temperature and pressure-less sintering process, where a possibly slight diffusion of native SiO_2 on the Si surface toward Ag is indicated by TEM observation, enabling the integration of Ag and Si into one continuous network. Owing to the robust well-bonded composite sintering, the Ag@Si joining strategy provides mechanical/microstructural reliability far beyond the pure Ag sinter joining, demonstrating significant prospects in high-temperature interconnection applications. During the harsh thermal cycling (−50–250 °C), the mitigating effect of the Si addition on CTE mismatch is manifested through the substantial suppression of microstructure deterioration in Ag@Si joint that occurs in pure-Ag-sintered joint, while the shear strength retention rate is doubled. Detailed investigation into the mechanism for elevated performance was conducted by material property and Missies stress analysis. The incorporation of Si helps modify the CTE, elastic properties, and stress distribution of Ag@Si-sintered material, synergistically contributing to the satisfactory joining reliability.

1. Introduction

The use of power converters has considerably increased over the past few decades, with a general trend of progress in the use of renewable energy. Third-generation wide band-gap (WBG) semiconductors, such as SiC, GaN, and Ga_2O_3, have revolutionized the use of power converters because of their high temperature and high power-density capabilities [1–3]. Although the high efficiency of WBG semiconductors has greatly benefited the miniaturization and versatility of power devices, it poses challenges in module packaging technologies. For example, the junction temperature could exceed 200 °C and even reach up to 300 °C in the application fields such as electric vehicles, aircrafts, and deep gas/oil extraction. Conventional tin-based solder alloys with melting points of 183 °C–230 °C can cause remelting issues, thus significantly compromising the functional reliability [4–7]. Additionally, the poor thermal conductivity of solders can limit the effective heat dissipation, reducing the overall efficiency of the module. As die-attached material play a critical role in signal transmission, heat dissipation, and mechanical support of power devices, their poor functioning must be resolved before applying them to WBG power devices on a large-scale [8–12].

With Tesla pioneering the use of Ag sintering die-attachments in the power modules of their Model-3 electric vehicles, Ag sinter joining has garnered even greater attention [13–17]. The Ag-sintering method outperforms various die-attached methods in terms of its high melting point (961 °C) and the superior electrical (63×10^6 S/m) and thermal (429 W/mK) conductivities of Ag among various metals [18–21]. Note that an ideal interconnect material should assure consistent

* Corresponding author.
E-mail address: chenchuantong@sanken.osaka-u.ac.jp (C. Chen).

https://doi.org/10.1016/j.compositesb.2024.111519
Received 14 February 2024; Received in revised form 24 April 2024; Accepted 1 May 2024
Available online 9 May 2024

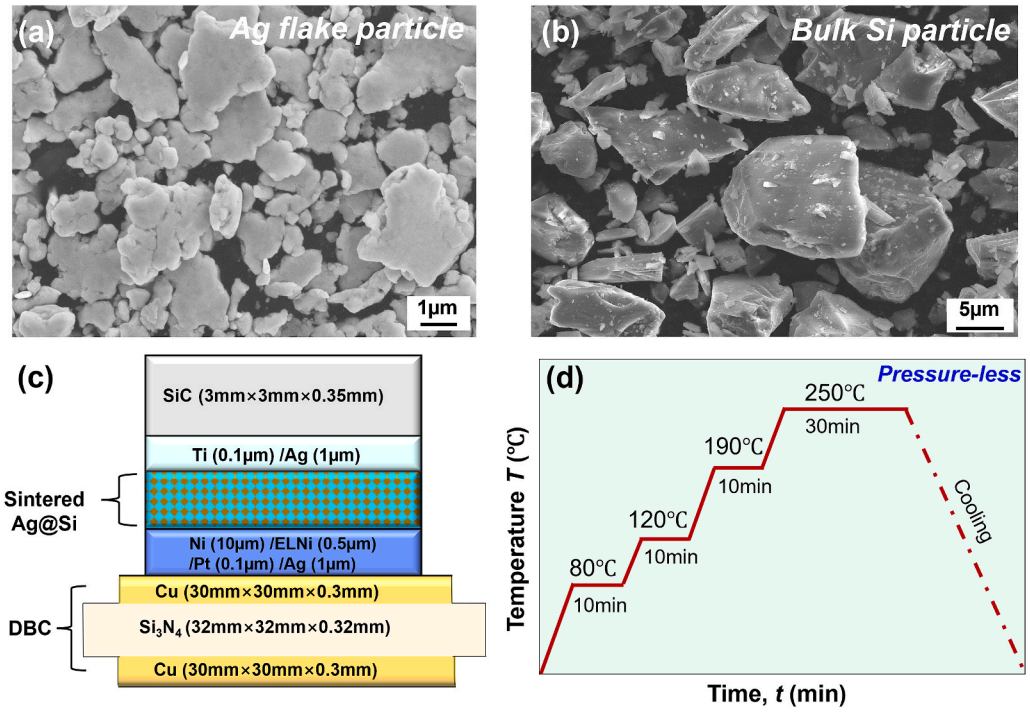

Fig. 1. FE-SEM images of pristine micron-sized (a) Ag flakes and (b)Si particles; (c) SiC/DBC die-attached structures bonded by hybrid Ag@Si sintering for reliability evaluation. (d) Low-temperature and pressure-less sinter joining conditions for Ag@Si hybrid paste joining.

performance in harsh environment and survive thermal shock cycles in addition to offering high service temperature and mechanical–electrical–thermal connections. However, the sintered Ag joining suffered degradation or performance deterioration due to thermomechanical stress [22–24]. Its use is hindered by the limitations of high cost and significant mismatch of the coefficient of thermal expansion (CTE) [25]. Currently, despite precedents (such as those proposed by Tesla), the use of 100% pure Ag die-attachment is challenging for most manufacturing industries, which involves a considerable rise in raw material expenses [26,27]. Therefore, some researchers have proposed the use of cost-effective Cu-sintered bonding. However, Cu requires a specific sintering atmosphere and displays subsequent oxidation issues, making its practical implementation even more difficult [28–30].

Moreover, the sintered Ag die-attached module encounters serious CTE mismatch, wherein Ag (18.4 ppm/K) possesses a much higher CTE value than its adjacent SiC chip (4.0 ppm/K) and Si_3N_4 ceramic substrate (3.2 ppm/K) [31,32]. It renders the Ag sinter-bonded device unable to survive temperature fluctuations, thus causing the overall device to fail [33–35]. During thermal shock cycles, severe CTE mismatch subjects an Ag-sintered joint to alternating tensile and compressive stresses resulting from the repeated expansion/contraction between components at different rates. Such thermomechanical stress could result in severe crack propagation, delamination, and interface plastic deformation, ultimately resulting in joint failures and poor reliability. Although certain commercial Ag pastes perform satisfactorily, it remains a significant challenge to realize a pure Ag-sinter interconnection with both good microstructural integrity and mechanical reliability under harsh thermal/power cycling conditions [36].

Rather than relying solely on pure Ag sintering, numerous Ag-based composite joining technologies were explored for cost-effective and long-lasting packaging service. Ag/Cu composite bonding emerges as a popular die-attach strategy, including Ag/Cu composite paste- and Ag/Cu alloy-based bonding, which accommodates a high Cu content (20–80 wt%) due to their good sinter-ability and compatibility [25,37–39]. However, the oxidation issue of Cu inevitably worsens the reliability during high-temperature operations. Other alternatives include the introduction of tiny amount of doping element (≤5 wt%), to reinforce the Ag sinter paste in terms of mechanical/thermal properties. Although thermal conductivity improved from the original 171.4 W/(m·k) to 240 W/(m·k) with 0.25 wt% graphene addition, and Young's modulus increased from 9.5 GPa to 13.4 GPa with 1.5 wt% SiC addition, satisfactory thermal shock reliability has not yet attained among these dual sintering structures up to date [40,41].

In this regard, this study presents a novel Ag@Si composite sinter structure, which utilizes micron Ag-flakes as fillers, coupled with micron Si particles as additives. The micron Ag flakes were employed because our prior studies have demonstrated its favorable sintering ability under no-pressure and low-temperature conditions [42–45]. Si was selected as the doping element because of its low cost and a low CTE value of 2.6 ppm/K [46,47]. Being the second most abundant element, Si is affordable enough to offset the high cost of Ag, thus elevating the cost effectiveness of the resulting device. Moreover, Si is expected to lower the CTE value of the Ag@Si joining layer. A closer match between the CTE of the joined layer and semiconductor chips/substrates is crucial for minimizing the thermomechanical stress of a die attachment, which mitigates the microstructure deterioration and the following reinforcement in mechanical strength [37,48]. This could improve the overall Ag-sintered packaging technology in terms of cost, microstructure stability, reliability, and durability.

As such, we developed the joint structure of SiC chip and direct bonding copper substrate (DBC) bonded by Ag@Si composite pastes containing varying Si ratios. The sintering process occurred at 250 °C under ambient pressure conditions. Comprehensive investigations were conducted as follows. (1) The reliability of Ag@Si joint materials was assessed using a harsh thermal-cycling test ranging from −50 °C–250 °C for 1000 cycles. (2) The CTE modification effect of Si was analyzed in terms of thermal expansion characteristics and mechanical properties (3) The stress distribution of Ag@Si joints was analyzed by finite-element model (FEM) simulations.

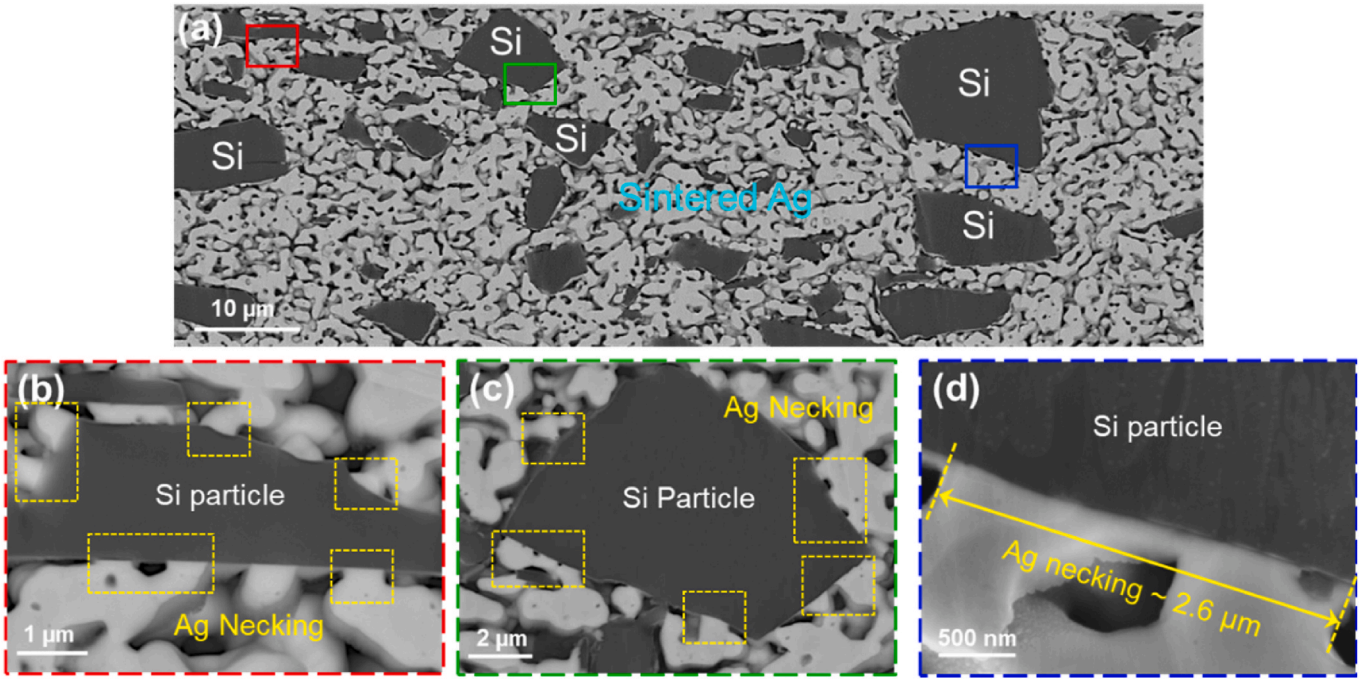

Fig. 2. (a) Cross-sectional view of the Ag@Si20% paste at the as-sintered state. (b), (c) and (d) The enlarged views of bonding conditions between sintered Ag and Si additives.

2. Material and methods

2.1. Specimen preparation

In this study, a composite Ag@Si paste was developed using micron-sized Ag flake particles (AgC-239, Fukuda Metal Foil and Powder, Kyoto, Japan) as fillers, with dimensional features of approximately 3 μm (diameter) × 250 nm (thickness), as shown in Fig. 1a. The Si particle additive was used following a simple mechanical ball-milling process, resulting in angular shapes with an average size of 10 μm, as shown in Fig. 1b. To analyze the effect of Si additives on the joining property of die attachment, composite pastes with two volume ratios of Si additives were prepared: 90%Ag–10%Si and 80%Ag–20%Si. These particles were then magnetically stirred in alcohol for 30 min, followed by ultrasonication for 30 min. An ether-type solvent (CELTOL-IA, Daicel Corporation) was employed as a suitable wetting agent for paste fabrication because of its satisfactory viscosity and good compatibility with Ag flake particles. The powder mixture was dispersed in the CELTOL-IA solvent by using a planetary mixer (HM-500, Keyence Corporation) for 3 min at 2000 rpm. The weight ratio of the Ag@Si powder to the CELTOL-IA solvent in all the pastes was controlled at 10:1, for a moderate viscosity level of 150–250 cPs. Hereafter, the composite pastes are referred to as Ag@Si10% and Ag@Si20% pastes. In addition, as the comparison group, a pure Ag-flake paste (denoted as Ag100% paste) was prepared using the same procedure without adding Si particles.

2.2. Die-attach structure fabrication

Dummy-grade SiC dies (3 mm × 3 mm × 0.35 mm) were employed for bonding to the DBC ($Cu/Si_3N_4/Cu$) with a dimension of 30 mm × 30 mm × 0.92 mm, thus forming a SiC/DBC die-attached structure, as depicted in Fig. 1c. The Si_3N_4-DBC substrates employed herein was obtained through the Active Metal Brazed (AMB) method with excellent thermal cycling resistance. Prior to the bonding process, all chips and substrates underwent a metallization treatment. For the die-attached structure used in the thermal aging test, 100-nm-thick Ti and 1-μm-thick Ag were sputtered onto both the SiC dies and DBC substrates. While the DBC substrate was deposited with a novel surface finish, referred to as electroplated Ni-combined with electroless Ni-/Pt-/Ag-(EN-ELNPA), comprising 10-μm electroplated Ni, electroless plated 500-nm Ni, 100-nm Pt, and 1-μm Ag. This deposition process has been reported in our previous study [49]. The robust EN-ELNPA surface finish has been proven to protect the substrate from plastic deformation during thermal cycling owing to the tough Ni layer and thereby provide a relatively stable joint structure to study the Si additive effect [50]. After metallization deposition, the as-prepared pastes were printed onto substrates via a metal stencil mask with a thickness of 100 μm. The chips were then mounted onto the pastes to form a joint structure. Finally, a low-temperature and pressure-less sintering was applied at 250 °C for 30 min for all the structures, as depicted in Fig. 1d.

2.3. Reliability evaluation and characterization

Prior to the reliability assessment, the interfacial connection between the Ag and Si in the as-sintered Ag@Si20% structure was first examined through scanning electron microscopy (SEM, SU8020, HITACHI), transmission electron microscopy (TEM, JEM- ARM200F, JEOL) and energy-dispersive X-ray spectroscopy (EDS). Next, the thermal shock reliability of the SiC/DBC joints was investigated using a thermal cycling chamber (TSE-11-A-S, ESPEC, Osaka, Japan). The thermal cycling test was implemented from −50 °C–250 °C with 30 min dwell at each extreme temperature up to 1000 cycles. The temperature switch between −50 °C and 250 °C was within 10 s. The evolution of microstructures and mechanical properties were systematically analyzed. The cross-sections were prepared at specific cycling points of 0 (initial state), 100, 500, and 1000 cycles by using an ion-milling polishing machine (IM 4000; Hitachi, Japan), and then used for SEM-based microstructural visualization. The shear strength of the die during thermal aging was measured using a shear tester (DAGE 4000 bonds tester, UK) at a shear rate of 50 μm/s. In addition, the crack evolution during thermal cycling was characterized using a three-dimensional (3D) computed tomography (CT) X-ray system (XVA-160 N, Uni-Hite System Corporation, Japan), which was equipped with a motor-driven sample stage and image acquisition technique. The tensile properties

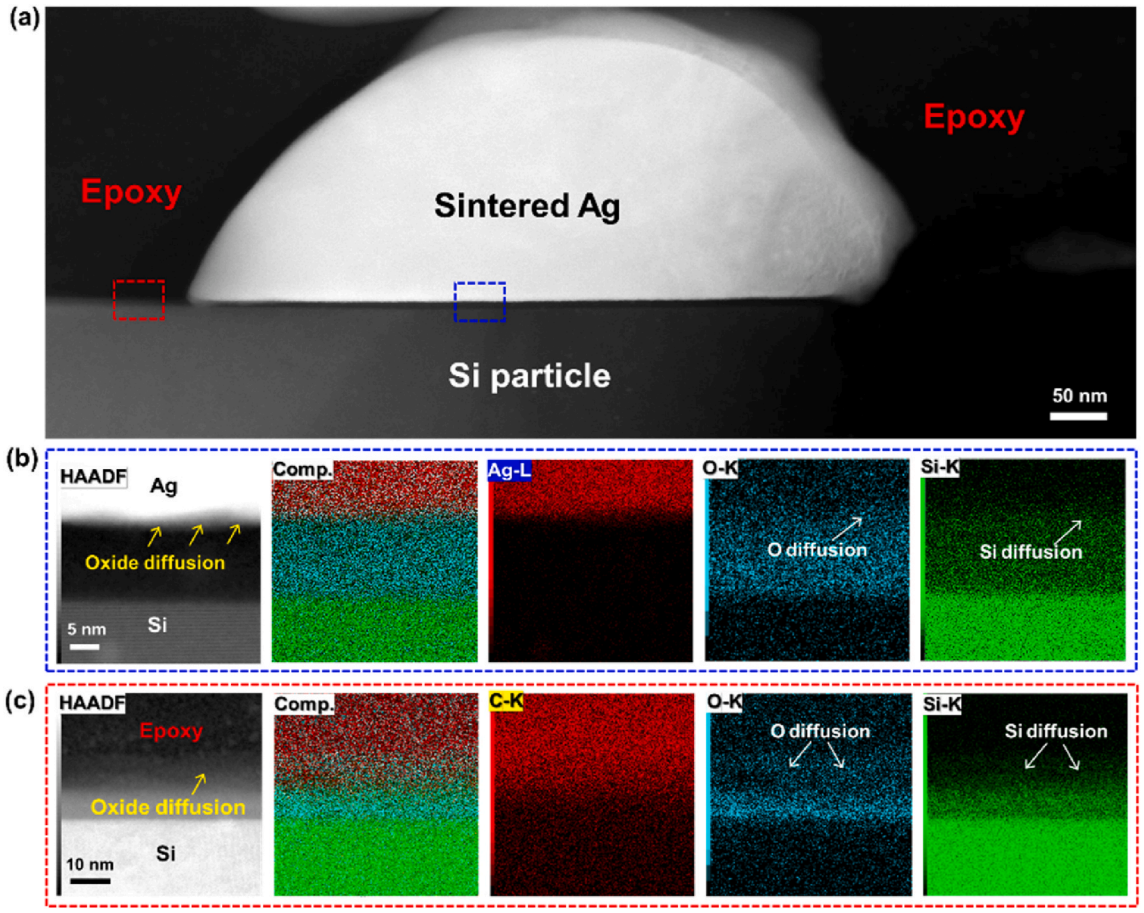

Fig. 3. (a) STEM observation of the interface between Ag and Si. HAADF and EDS mapping analysis of the (b) Ag/Si interface and (c) epoxy/Si interface.

and CTE of the sinter pastes were measured using a micro-force testing system (Tytron TM 250, MTS system Corp.) and thermomechanical analyzer (TMA, Netzsch Co.), respectively. All the test specimens were prepared by sintering the pastes at 250 °C for 30 min under ambient air conditions.

In addition, reasonable modeling parameters are essential prerequisites for obtaining reliable FEM simulation results. The details of FEM simulation are given below: to accurately characterize voids, the mesh near the bonding layer is the densest, i.e., 0.5 μm. To minimize the total mesh count, the mesh density gradually decreases from the bonding layer outward, transitioning from finer to coarser. Specially, 0.5 μm at Ag/Ag@Si sinter layer, 0.5 μm at the both Ag- sputtered and Ni-/Ag- plating layers, and range from 0.5 to 10 μm within the Si chip and DBC substrate areas. The boundary condition is defined as: left edge Ux = 0; bottom edge Uy = 0; utilizing a 1/2 Symmetry model. The classical elasto-plasticity-isotropic hardening model serves as the functional equation in this study.

3. Results: analysis of Ag@Si composite interface

In the context of a composite joined material, the condition of heterogeneous interfaces is highly significant, as these interfaces represent vulnerable areas, where various defects can readily occur [51]. Therefore, the interface of sintered Ag/Si additives in the Ag@Si sintering structure must be confirmed before the reliability evaluation. Fig. 2a exhibits the cross-sectional view of an initially sintered Ag@Si20% joining layer. In the uniform Ag microporous network, irregular Si particles with sizes of approximately 1–10 μm were randomly dispersed. Multiple locations containing the Ag/Si interface were examined, as shown in Fig. 2b–d. Fig. 2b and c shows the formation of a narrow and elongated Ag necking around the Si particles for bridging the porous, sintered Ag with Si. Fig. 2d shows that the connective ratio could even reach up to ~2.6 μm, suggesting the formation of robust Ag@Si bonding. SEM observations reveal the formation of a composite sintering network with Ag and Si closely bonded to each other with almost no visible gaps.

The Ag/Si interface was further examined through STEM-EDS observations. The thin film specimen was prepared by polishing the Ag@Si20% sintered material under a cured epoxy resin support. Fig. 3a shows an Ag/Si interconnective region surrounded by the epoxy support. Detailed elemental analyses were conducted on both the Ag/Si interface and the epoxy/Si interface. In Fig. 3b–a distinct intermediate layer of approximately 10 nm thick was observed between the Ag sintered neck and Si through High-Angle Annular Dark-Field (HAADF) imaging. According to the EDS mapping analysis, the distribution of Ag, O, and Si elements can be differentiated, with the prominent O element located in the middle, identifying the intermediate layer as SiO_2. Further details of the Ag/Si bonding interface are displayed in the Supporting Information (SI) Fig. S1. Fig. S1a reveals the visible presence of a uniform middle layer. The sandwich bonding structure at interface, with two crystalline layers closely adhered to a middle amorphous layer, is more clearly discernible in HRTEM in Fig. S1b. Finite Fourier transform (FFT) diffraction patterns distinctly matched the lattice features to Ag [110] and Si [110] facets, respectively. The SiO_2 layer could originate from the native passivation layer on the Si surface. TEM analysis revealed that sintered Ag and Si remain tightly integrated even at the nanoscale level. Interestingly, a new contrast layer has emerged at the interface between SiO_2 and Ag, indicating a change in the average atomic mass in this region. Further supported by EDS mappings, it is evident that within the new contrast layer, the concentration of O and Si elements are higher than that in the sintered Ag layer, indicating the

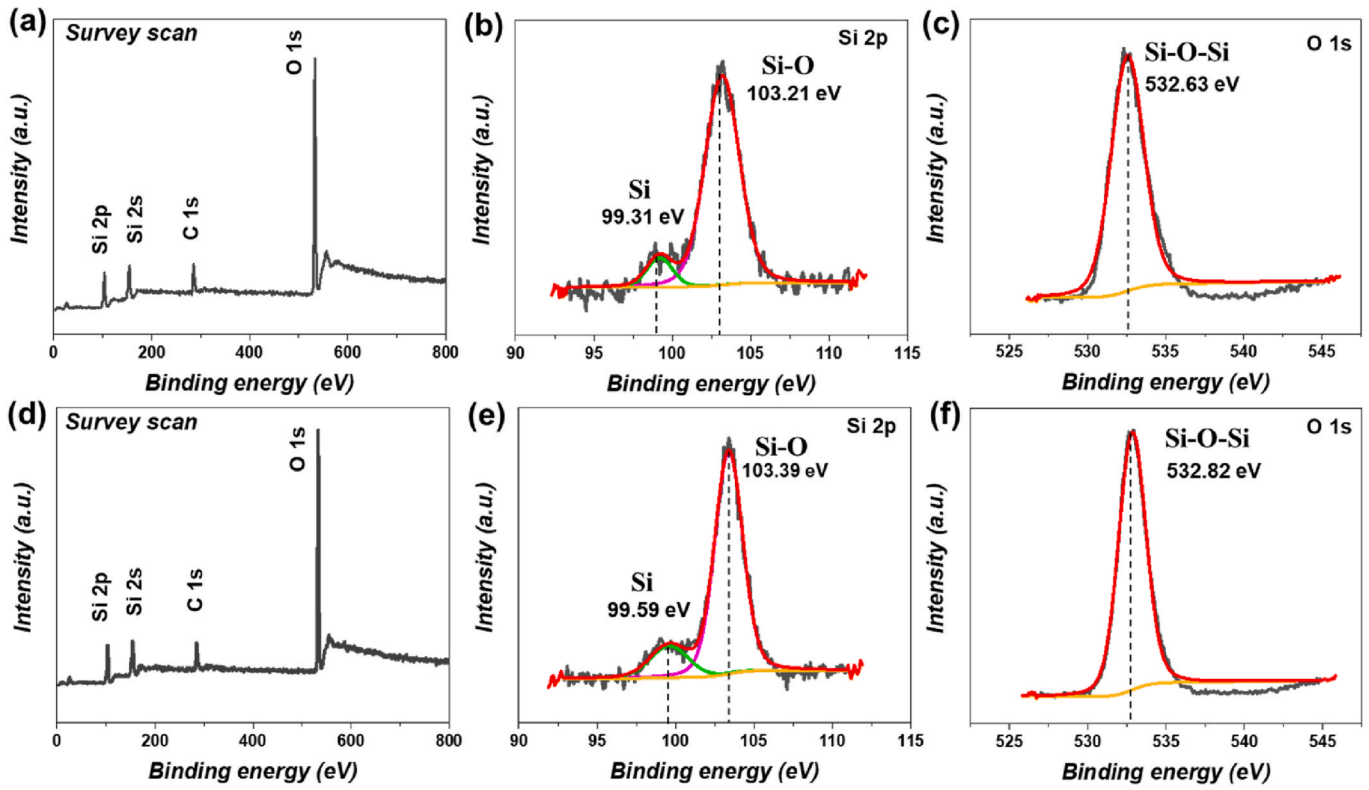

Fig. 4. XPS survey scan, deconvoluted peaks of Si 2p and O 1s spectra of Si additive particles. (a–c) pristine Si; (d–f) Si particles after heat treatment.

slight diffusion of SiO_2. Additionally, an intermediate layer of SiO_2 is also present at the epoxy/Si interface in Fig. 3c–and a subtle change in contrast is observed in the region of its junction with the epoxy. Meanwhile, the diffusion of O and Si elements toward epoxy was revealed by EDS mappings.

Based on the results of TEM analysis, it appears that there might be a slight diffusion of SiO_2 into Ag, which is attributed to the possible growth or rearrangement of the SiO_2 passivation layer caused by the sintering process. This would favorably contribute to the reinforcement of the bonding interface. The well-integrated Ag@Si sintering network might be formed as follows: during the sintering process, substantial recovery and reshaping may take place in Ag flakes, transforming them from a flat sheet to a spherical morphology, as reported previously [52]. This leads to the exposure of multiple fresh silver surfaces. Simultaneously, the SiO_2 layer diffuses into these surfaces through slight growth or rearrangement, ultimately forming a sturdy bonding structure. Herein, being different from a simple physical mixture between heterogeneous substances, the Ag@Si network formed based on SiO_2 diffusion offers a mechanically stronger matrix, laying the foundation for achieving a robust and close CTE-matched composite joint.

XPS studies were conducted on Si additive particles, both in their pristine state and after heat treatment under the same conditions as sintering process (i.e., 250 °C for 30 min in air), to confirm their surface condition. Fig. 4a demonstrates the survey scan spectrum of pristine Si particles, clearly indicating the presence of C 1s, O 1s, and Si 2p. Deconvolution of Si 2p spectra in Fig. 4b shows two main chemical states corresponding respectively to a Si at 99.31 eV and Si–O bond at 103.21 eV. The O 1s at 532.63 eV also fitted well with the characteristic peak of Si–O–Si as shown in Fig. 4c. These verify the presence of SiO_2 passivation layer in the pristine state. Fig. 4d–f exhibits the XPS spectra analysis of Si particles after the heat treatment. Compared with the initial state, spectra are not very different, which also indicates that changes such as growth or rearrangement of SiO_2 layer during sintering are relatively minor.

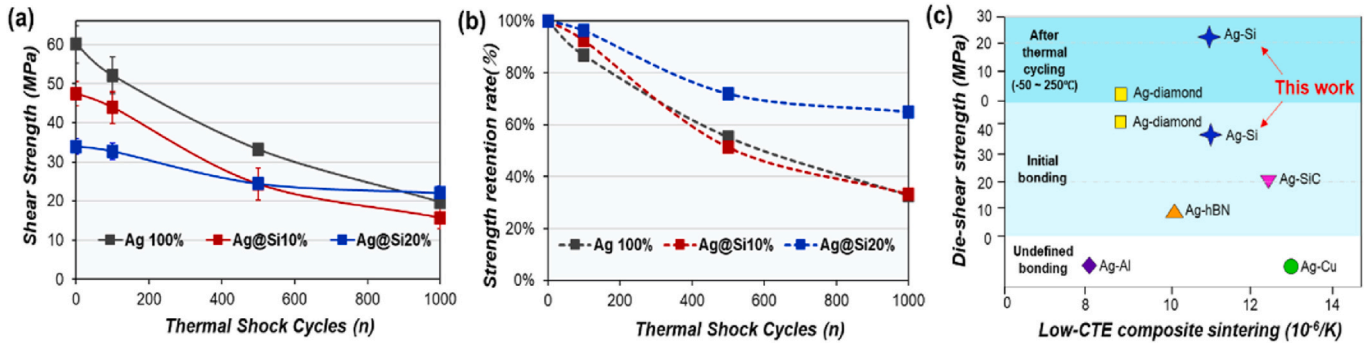

Fig. 5. (a) Die-shear strength of joint structures produced by sintering of Ag100%, Ag@Si10% and Ag@Si20% pastes during thermal shock cycles. (b) Strength retention of each joint based on ratio of actual strength to initial strength. (c) Shear strength distribution of low CTE die-attached systems prepared by compositing Ag with different materials.

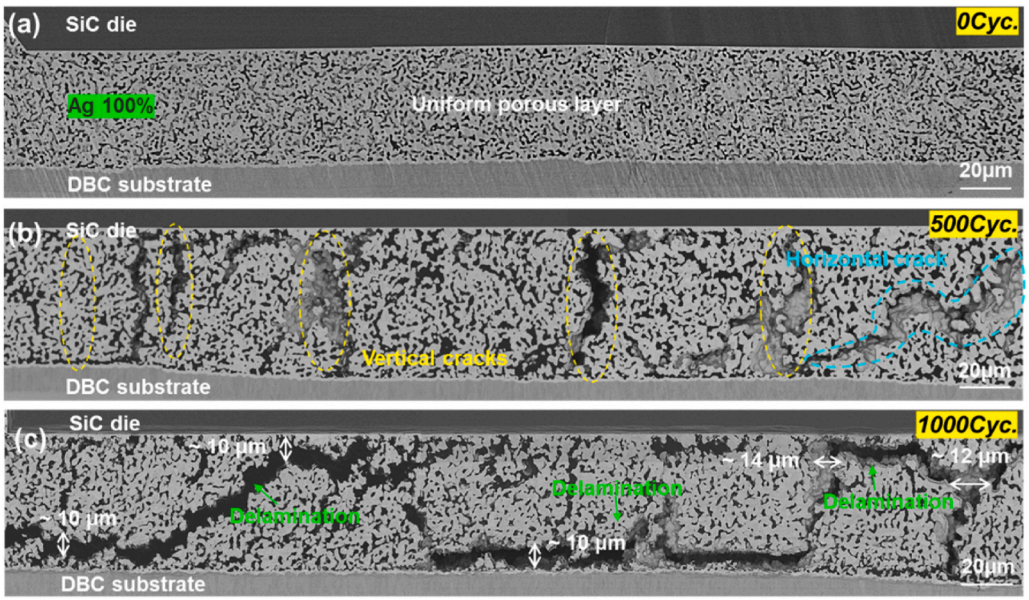

Fig. 6. Microstructure changes in the cross-sections of Ag100% joint structure during thermal cycling period: (a) at initial state, (b) after 500 cycles (c) after 1000 cycles.

4. Results: reliability evaluation

4.1. Shear strength of Ag@Si joints

Fig. 5a shows the die shear strength of joint structures formed by three sinter pastes (Ag100%, Ag@Si10%, and Ag@Si20%) during thermal cycling. The result showed that Si additives cause a gradual drop in strength at the initial state, where the as-sintered strengths for the Ag100%, Ag@Si10%, and Ag@Si20% joints were evaluated as 60.10, and 47.53, and 33.99 MPa, respectively. The initial strength reduction in Ag@Si joints could be attributed to the doping effect of heterogeneous Si element.

Unsurprisingly, the Ag100% joint experienced a rapid bonding deterioration from the initial 60.10 MPa–33.21 MPa after 500 thermal cycles, and further decreased to 19.73 MPa after 1000 cycles. The Ag@Si10% joint also exhibited a similar declining trend in strength, retaining only 15.76 MPa of the strength after 1000 cycles. In contrast, despite having the lowest initial bonding strength among all structures, Ag@Si20% exhibited the highest bonding strength of 22.07 MPa after 1000 cycles. These results suggest the high strength-retention capability of the Ag@Si20% joint, as clearly demonstrated in Fig. 5b. Ag100% and Ag@Si10% joint structures exhibited poor capability of retaining their original strength over repeated cycles, with strength-retention rates of only 32.82% and 33.15%, respectively, after 1000 cycles. However, the Ag@Si20% joint consistently showed a much higher retention rate, up to 64.93% at 1000 cycles, which is twice that of the Ag100% joint. These findings indicate that the Ag100% joint suffered significant buildup of thermal stress, and the addition of 10% Si appeared to have no obvious impact on the stress buildup. The Ag@Si20% joint is clearly more resistant to the strength weakening induced by thermal cycling, implying a thermal stress-alleviated effect.

To date, few composite die-attached systems have been developed by modifying Ag pastes through the incorporation of different low CTE elements, including Al, SiC, hBN, and diamond [37,53–55]. The challenge lies in not only reducing the CTE but also preserving the mechanical property of the die-attached structure at the meantime. Fig. 5c summarizes the distribution of the die-shear strength in the low-CTE composite sinter joints. Although the CTE of the composite sintering materials can be effectively modified, with values dropping to as low as ~8 ppm/K in the Ag@Al and Ag@diamond sintered composites, the mechanical strength was significantly compromised. Owing to the poor initial strength, most studies have limited their investigation of mechanical properties to the initial bonding stage. The Ag@diamond joint, with a high initial strength of 43.8 MPa, demonstrated a residual strength of only 3.7 MPa after 1000 thermal cycles from −50 °C to 250 °C, resulting in a complete detachment of the joint structure. These sintering composites consist of a simple physical mixed structure, which is mechanically unstable and fails to show any CTE-mismatch mitigation effects under harsh environment. Herein, the proposed Ag@Si composite sinter joint could simultaneously achieves low CTE and favorable bonding strength retention of 22.07 MPa, surpassing that of the pure Ag sinter joint. The substantial increase in mechanical strength is mainly attributed to the formation of an integrated Ag@Si sintering network, providing a mechanically stable bonding framework that enables stress relief effects.

4.2. Microstructure-evolution analysis

A wide range of cross-sectional observations were made on the overall joint structures for comprehensive evolving information. Fig. 6 showcases the microstructure evolution of the Ag100% joint at the initial stage, after 500 cycles, and after 1000 cycles of thermal cycling. From the as-sintered state (Fig. 6a) to after 500 cycles (Fig. 6b), the Ag100% joined layer was significantly damaged, i.e., the formation of coarsened Ag particles, vertical/horizontal cracks running through the bonding layer. As such, the mechanical strength rapidly reduced to approximately 50% of its as-bonded state. After 1000 cycles, Fig. 6c displayed a more serious delamination phenomenon along the upper and bottom bonding interfaces, with a separation distance reaching ~10 μm at both bonding interfaces. Apparent interfacial debonding undoubtably resulted in the further reduction of the shear strength, as evidenced by the finally poor strength retention rate of 32.82%. Owing to the EN-ELNPA protective layer, the bonding interfaces with DBC substrate could remain flat without any obvious deformation until 1000 thermal cycles. Therefore, the thermomechanical stress in the Ag100% joint was released primarily through the propagation of large cracks, triggering severe debonding and greatly compromising the integrity of the Ag100% joint.

Subsequently, the microstructural changes in the Ag@Si composite joints were also analyzed. The Ag@Si10% joint maintained better

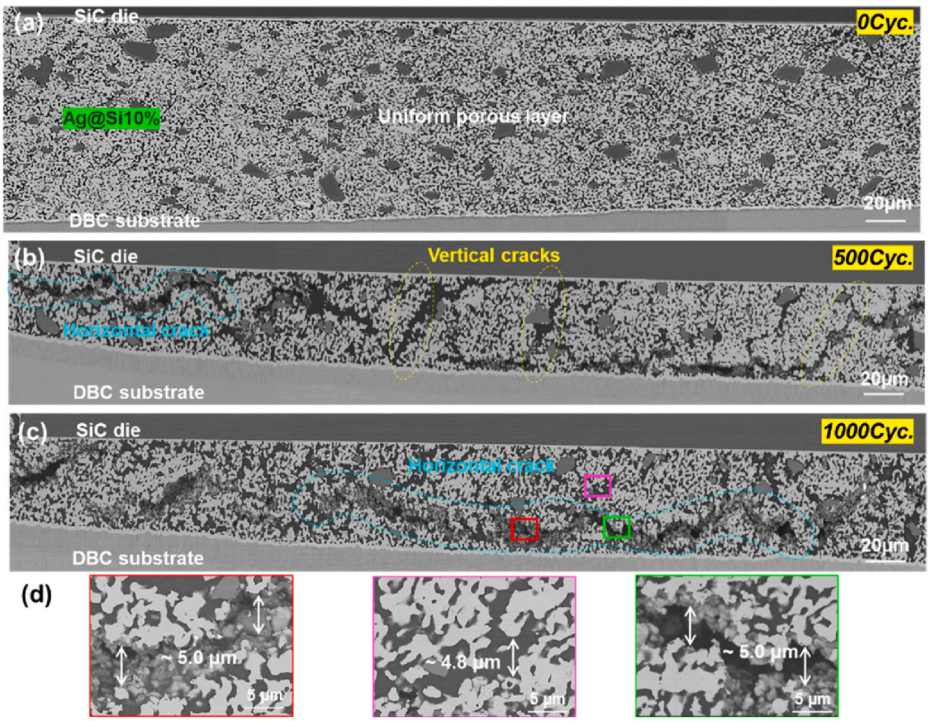

Fig. 7. Microstructure changes of cross-sections in the Ag@Si10% joint structure during thermal cycling period: (a) at initial state, (b) after 500 cycles, (c) after 1000 cycles. (d) The enlarged views of cracking growth after 1000 cycles.

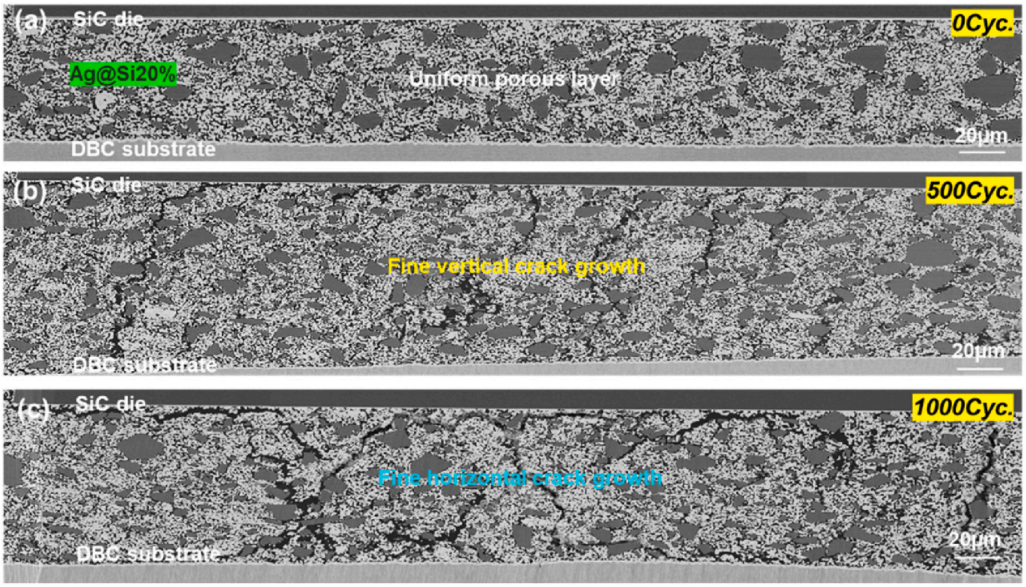

Fig. 8. Microstructure changes in the cross-sections of Ag@Si20% joint structure during thermal cycling period: (a) at initial state, (b) after 500 cycles (c) after 1000 cycles.

integrity as only crack growth was observed in the vertical/horizontal directions after 500 and 1000 thermal cycles, as depicted in Fig. 7a–c. The extension of long horizontal cracks explain its rapid decline in bonding strength. In addition, the crack reduced to approximately 5 μm in width, along with inhibition of the interfacial delamination as shown in Fig. 7d. Although the mechanical reliability of Ag@Si10% joint did not differ much from that of the Ag100% joint, there is a clear improvement in microstructural integrity, suggesting the effect of CTE modification on thermo-mechanical stress mitigation. However, it is likely due to the less amount added, the stress-alleviated effect is limited and cracks as wide as 5 μm can also lead to a rapid decrease in strength. Thus, 10% Si addition failed to show an effect on the mechanical reliability.

Interestingly, the microstructure of Ag@Si20% joint almost maintained its homogeneity and integrity throughout the thermal cycling process, without any typical drastic evolutions. The minor deteriorations involved a few fine, short vertical cracks formed after 500 cycles and additional horizontal cracks at the upper bonding interface after 1000 cycles, as shown in Fig. 8a–c. The satisfactory microstructure integrity allows the Ag@Si20% joint structure to possess the highest strength-retention rate among the studied three structures. A difference in joint thickness existed due to the manual mounting process. The

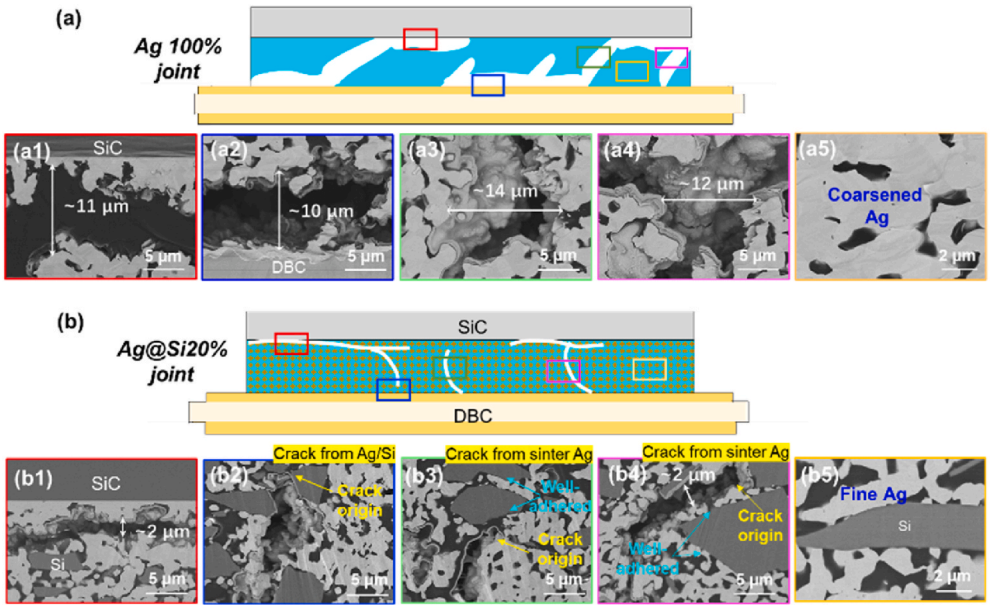

Fig. 9. Comparative schematic drawing of the microstructure evolution between (a) Ag100% joint and (b) Ag@Si20% joint structures after 1000 thermal cycles. (a1-a5) and (b1-b5) are the evolving details at multiple locations within both joint structures, respectively.

thickness of most joints falls within a 50–70 μm range, considered reasonable and minimally impacting the thermal fatigue, provided sufficient test specimen are available. It is worth noting that the shear strength is an average value obtained from 7 samples, effectively mitigating the impact of few exceptionally thick joints. Thereby, it is believed that the mechanical/microstructural evolution trends of each type of joint are credible to reflect their thermal fatigue behaviors.

Fig. 9 shows a comparison of the microstructural changes between Ag100% and Ag@Si20% joints after 1000 thermal cycles, along with evolving details at various locations. As shown in Fig. 9a and b, the fatigue characteristics of the sintered Ag microstructure largely changed with the incorporation of 20% Si. In other words, not only did the number and size of cracks decrease but the interfacial debonding was also suppressed. Specifically, in the Ag100% joint, the average width of the vertical cracks and horizontal delamination exceeded ~10 μm, as shown in Fig. 9a1–a4. As reported, the presence of large voids (measuring ~500 nm in diameter) and Kirkendall delamination (measuring ~1 μm in width), would directly impact mechanical integrity and heat dissipation of joint structures from top to bottom [56,57]. Likewise, an interfacial delamination as wide as 10 μm would inevitably cause greater damage on the mechanical/thermal properties of Ag100% joint. Furthermore, these vertical cracks and horizontal delamination were interconnected, causing the Ag100% joined network to be incomplete and disconnected, thus resulting in premature detachment. In contrast, with the increase in Si content, the crack width was observed to narrow from over 10 μm in the pure Ag joint to ~5 μm in the Ag@Si10% joint and further to ~2 μm in the Ag@Si20% joint, as shown in Fig. 9b1–b4. The finer cracks were relatively independent of each other, allowing the Ag@Si20% joining layer to remain intact. The gradually strengthened microstructure strongly suggests the role of Si additives in alleviating stress buildup.

Additionally, as a CTE mismatch also exists between the sintered Ag

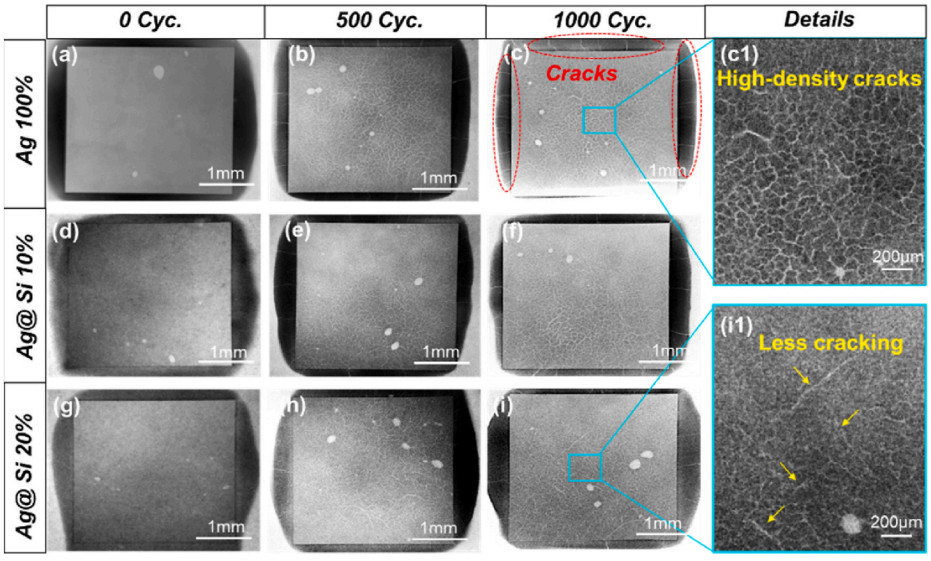

Fig. 10. X-ray CT images of three types of die-attached structures at initial, 500 cycles and 1000 cycles: (a–c) Ag100%, (d–f) Ag@Si10%, (g–i) Ag@Si20%; (c1) and (i1) are the magnified details of evolution in the Ag100% and Ag@Si20% joint structures after 1000 thermal cycles.

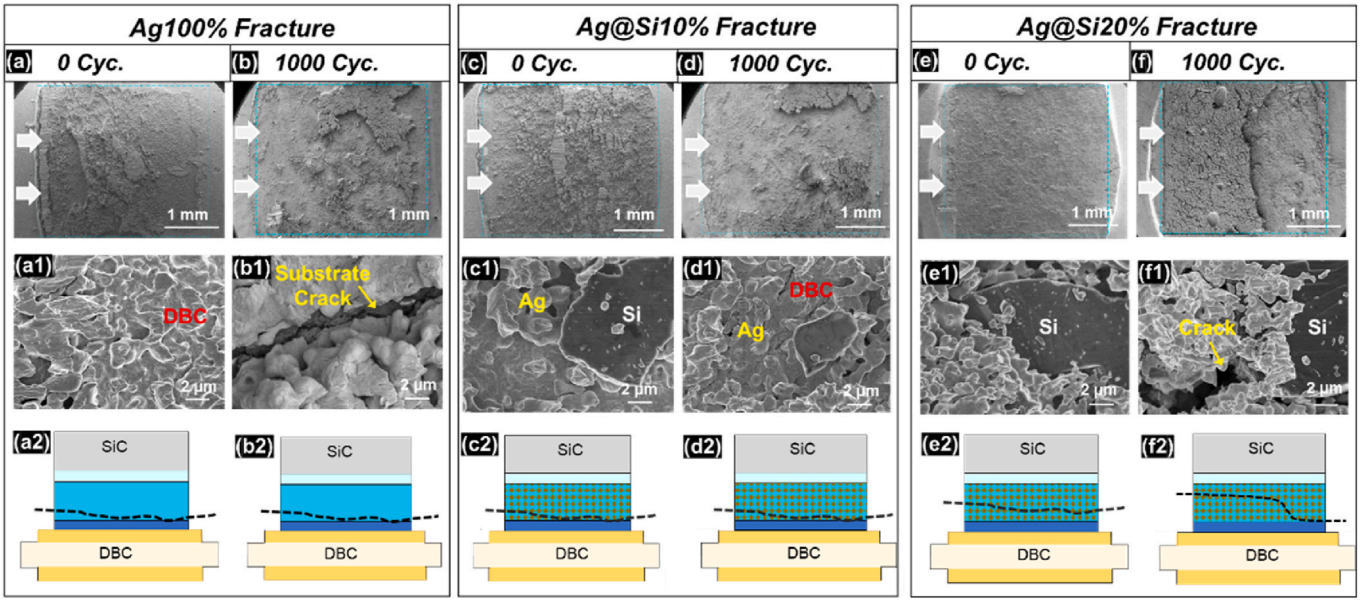

Fig. 11. The fracture surface morphology, magnified details and schematic plot of the joints before and after 1000 thermal cycles; (a-a2) and (b-b2) for the Ag100%; (c-c2) and (d-d2) for the Ag@Si10% joint; (e-e2) and (f-f2) for the Ag@Si10% joint.

and Si additives, the resulting stress may preferentially initiate the defects along the Ag/Si interface. Therefore, we carefully investigated the origin and propagation of cracks. Fig. 9b2 shows a crack originating from the Ag/Si interface. However, as depicted in Fig. 9b3 and 9b4, many cracks originated and propagated exclusively in the region of pure sintered Ag. Moreover, Si particles near the cracks still retained their bonding with the sintered Ag, indicating the mechanical stability of the Ag@Si composite sintering against thermal stress. Based on these observations, there is no evidence to suggest that cracks preferentially occurred along the Ag/Si interface; instead, they tended to grow randomly under the driving force of thermal stress. When comparing Fig. 9a5 and Fig. 9b5, visible grain coarsening is found in the Ag100% joint, while Ag grains in the Ag@Si20% joint maintain a fine structure, indicating the impeding effect of Si addition for Ag thermal motions. Moreover, the Ag and Si particles are still well connected after 1000 thermal cycles.

The X-ray CT observation shown in Fig. 10 offers a nondestructive, full-chip scale detection of structural deterioration. As shown, the three as-bonded structures demonstrated few fine voids, which could be attributed to the incomplete evaporation of solvents during the initial sintering process. Although all joints achieved well-established interface bonding, crack growth was particularly pronounced in the Ag100% joint. Fig. 10a–c shows dense crack propagation after 500 thermal cycles, which further extended to the overflowed area around the chip after 1000 cycles. The dense spiderweb-like pattern of crack propagation is more clearly displayed in Fig. 10c1, corresponding to multiple cracks observed in the cross-sections. By comparison, Fig. 10d–f shows that after 1000 cycles, the spiderweb-like pattern of cracks in the Ag@Si10% joint becomes less dense, as indicated by the fewer cracks in the cross-sectional views in Fig. 7. In the case of the Ag@Si20% joint, the crack propagation in both the chip-bonding and overflow areas was visibly reduced, as shown in Figs. 10g–11i. Fig. 10 c1 and 10i1 evidently demonstrate the crack-inhibiting role of the Si additive, as only sparse cracks existed in the Ag@Si20% joint instead of the dense spiderweb pattern. Cross-validation by X-ray CT detection and SEM observations confirmed the efficacy of the Si additive in mitigating microstructural degradation of Ag sintering.

4.3. Fracture behavior analysis

The fracture surfaces are crucial to provide valuable information related to the failure mechanisms. Fig. 11 presents the fracture analyses for the three joint structures. In the Ag100% joint, the initial fracture surface exhibited an uneven texture with Ag grains piled on the metallized DBC substrate (Fig. 11a and a1). This result corresponds to the failure route along the joined layer/metallized DBC interface, as illustrated in Fig. 11a2. After 1000 cycles, the fracture surface in Fig. 11b–b1 still show the residue of some coarsened Ag particles. In addition, large cracks appeared in the EN-ELNPA metallized layer on the DBC substrate, which could be attributed to the occurrence of through-thickness cracks in the cross-section. The severe deterioration at the interface, involving factors, such as substrate damage and delamination, contributed to a continued fracture route at the joined layer/metallized DBC interface (Fig. 11b2).

Fig. 11c–c2 and Fig. 11d–d2 shows that in the Ag@Si10% joint, both before and after thermal cycling, a fracture mode similar to that in the Ag100% joint is observed along the joined layer/metallized DBC interface. However, the unaffected and intact EN-ELNPA metallization layer implies stress relief (Fig. 11c1 and 11d1). Furthermore, a different fracture pattern was observed inside the joining layer in the Ag@Si20% joint structure. Fig. 11e–e2 show that the initial fracture surface exhibits a smooth texture and displays remnants of the Ag@Si sintered layer. The inner fracture mode is likely due to the increased brittleness of the Ag@Si20% joined materials, which is induced by the hindrance of Ag atom mobility due to the addition of 20% Si. After 1000 thermal cycles, Fig. 11f–f2 show that the remaining Ag@Si layer on the fracture surface visibly increased in thickness, suggesting a fracture route closer to the joined layer/SiC interface. This may be attributed to the extension of horizontal cracks at the interface with SiC, as revealed in the cross-section in Fig. 8c. Moreover, Fig. 11f1 shows that near the exposed cracks within the joined layer, Ag and Si still retain close contact, further confirming that not all cracks primarily originated along the Ag/Si interface.

The crack origin trend in Ag@Si20% joints was also confirmed by evolution of fracture surfaces as shown in SI Fig. S2. After 500 cycles, Fig. S2a shows early crack origin within both the pure sintered Ag and Ag@Si areas, consistent with the cross-sectional observation (See Fig. 8b), wherein the crack in pure sintered Ag area appeared even much

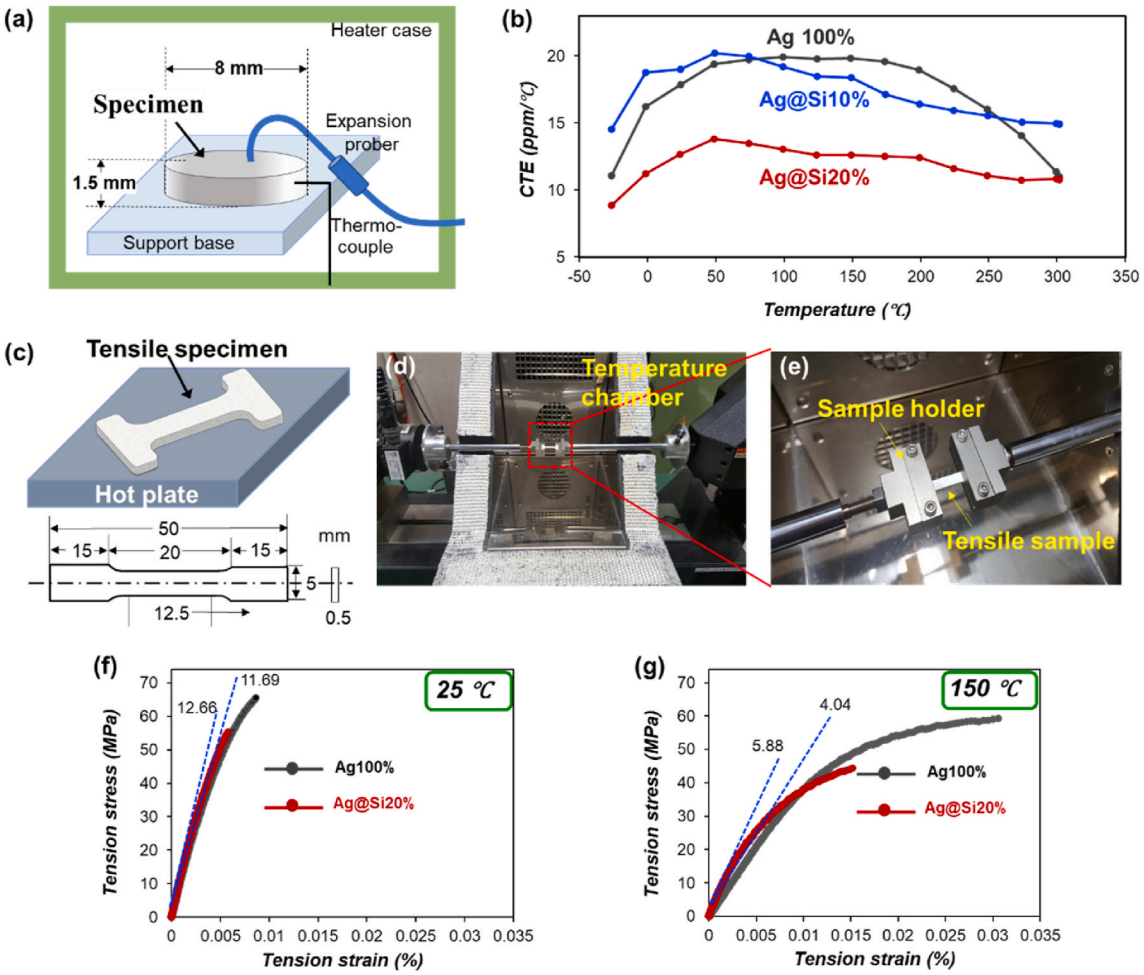

Fig. 12. (a) Schematic plot of the CTE measurement system and the dimensional depiction of disc-shaped specimen prepared by paste sintering. (b) CTE testing of Ag@Si sintered materials over a temperature range of −25 °C–300 °C. (c) Schematic diagram of the dumbbell-shaped sintering specimen for tensile testing with a detailed size description. (d) The micro-force testing system equipped with a flexibly controlled temperature chamber. (e) The sintered specimen fixed on the sample holder. Tensile stress-strain behaviors of Ag100% and Ag@Si20% sintered materials at (f) room temperature and (g) 150 °C.

more prominent. Moreover, in the enlarged Ag@Si areas (Figs. S2b and c), many sintered Ag particles remained on the Si surface even after the forceful die shearing, indicating the combination between Ag and Si should be more than the simple physical contact. After 1000 cycles, the crack within pure sintered Ag area evidently grew largely (Fig. S2d). Fig. S2e further shows that near the crack, the Si particles maintain good adhesion with the sintered Ag. These fracture details beneficially evidence the formation of mechanically stable Ag@Si composite sintered structure. In addition to the influence of microstructure evolution, different fracture behaviors suggest changes in material properties, as discussed in the next section.

5. Discussion

5.1. Material property analysis

The results of the analysis presented in previous sections collectively point to a thermal stress-mitigating effect of Ag@Si sintering in terms of improved mechanical and microstructural stability, including shrinking cracks, suppressed substrate damage, and delamination. The mechanisms for stress mitigation are explored according to material property analysis (e.g., CTE and mechanical properties) and stress distribution simulation.

Fig. 12a shows the schematic of the experimental setup for CTE characterization, wherein a disc-shaped sintering specimen with a thickness of 1.5 mm and a diameter of 8 mm was prepared. The measurements were performed from −25 to 300 °C at a heating rate of 5 °C/min. Fig. 12b plots the CTE variation trend of the three joined materials, namely Ag100%, Ag@Si10%, and Ag@Si20%. At lower temperatures, the addition of 10% Si exhibits a limited impact on CTE, while contributing to a reduction in CTE within the temperature range of 150–250 °C. As shown, 20% Si exhibited a more pronounced doping-effect, resulting in a much lower CTE for Ag@Si20% sintering. Moreover, the Ag100% specimen displays a reduction in CTE after 175 °C. This change might be attributed to the heat-treatment during CTE testing, which may serve as an additional sintering process, inducing slight thermal shrinkage in the Ag sinter structure. This effect would, to some extent, mitigate thermal expansion behavior [58]. Specifically, at 250 °C, the CTE was 16.03 ppm/K of the original Ag100% specimen. This value changed to 15.55 ppm/K in the Ag@Si10% sintering structure and significantly dropped to 11.08 ppm/K in the Ag@Si20% sintering structure. Hence, a much closer match was achieved in CTE of the Ag@Si20% joined structure, which displayed lesser differential expansion/contraction between components, consequently demonstrating a lower tensile/compressive stress theoretically. This is clearly one of the key factors leading to the improved reliability and overall performance of the Ag@Si20% joint.

Owing to the distinct difference in the bonding properties between the Ag100% and Ag@Si20% joints, their tensile behaviors were investigated at different temperatures. Fig. 12c shows the dumbbell-shaped

Table 1
The comparison in material properties between Ag100% and Ag@Si20% sintered materials.

Temperature	Material	Thermal expansion coefficient (ppm/°C)	Fracture strength (MPa)	Young's Modulus (GPa)	Yielding strength (MPa)
25 (°C)	Ag100%	17.87	97.46 ± 2.0	11.69 ± 0.3	59.46 ± 2.8
	Ag@Si20%	12.66	76.31 ± 8.3	12.66 ± 0.8	–
150 (°C)	Ag100%	19.84	80.88 ± 7.0	4.04 ± 1.7	44.47 ± 3.3
	Ag@Si20%	12.61	69.02 ± 2.1	5.88 ± 0.4	34.38 ± 1.2

specimen used for tensile testing with a detailed dimensional depiction. The micro-force testing system equipped with a controllable temperature chamber was utilized (see Fig. 12d and e). Young's modulus was calculated by dividing stress by strain, and the yield stress was determined based on the 0.2% offset yield strain. Table I summarizes the obtained material properties including CTE, fracture strength, Young's modulus, and yield strength. Fig. 12f shows that at 25 °C, similar Young's modulus values were evaluated as 11.89 ± 0.3 and 12.36 ± 0.8 GPa in the sintered Ag100% and Ag@Si20%, respectively. The original sintered Ag exhibited greater ductility with a yielding strength of 59.46 MPa, whereas the Ag@Si20% structure displayed no well-defined yielding point because of rapid fracture. That is, the incorporation of Si did not significantly modify the sintered Ag in terms of the elastic property at room temperature but led to a decrease in material ductility. The decrease in both fracture stress and strain suggested reduced ductile deformation prior to failure in Ag@Si20% compared to pure Ag sintering, as well as the increased brittleness. As the plastic deformation is obtained primarily owing to the dislocation motions and grain boundary sliding for metallic materials [59]. Note that the typical grain coarsening did not occur in the Ag@Si20% sintering during thermal cycling, as the presence of Si hindered atomic migration, recrystallization and grain boundary movements. Such hindering-effect would also work under applied stress during tensile test. In Ag@Si20% sintering, since most of sintered Ag adheres to Si, the restricted movements of grain boundary and dislocation render poor plastic deformation before fracture. The reduced plastic behaviors may then result in a fracture inside the main body of Ag@Si20% layer, differing from the fracture modes in other initial joints.

Fig. 12g shows that at 150 °C, both joined materials exhibited reduced fracture strength and Young's modulus, with values of 4.04 ± 0.7 and 5.88 ± 0.4 GPa for sintered Ag100% and Ag@Si20%, respectively, while displaying a more obvious ductile deformation. This could be attributed to the softening nature of the sintered Ag at elevated temperatures. The slight increase in Young's modulus allows a favorable trend of enhanced resistance to elastic deformation under low applied stress. However, a more pronounced and detrimental change is observed under further applied stress: both yield and fracture strength of sintered Ag@Si20% declined obviously at 25 °C and 150 °C. This demonstrates that, despite a well-integrated Ag@Si20% structure, its inherent material strength still falls short of pure Ag sintering, resulting in lower ductility and poorer fatigue resistance under the same stress levels. However, a clear increase in thermal fatigue resistance was achieved in the Ag@Si20% joint, indicative of the mitigated thermal stress by closer-matched CTE effect. The modifying effect on thermal stress is further analyzed by FEM simulation in the following section.

5.2. Stress-simulation analysis

The FEM simulation was used to study the impact of Si additive on the Mises stress distribution within joint structures. The Mises stress, which represents the cumulative effect of tensile, compressive, and shear stresses caused by temperature changes, is a valuable parameter for analyzing fatigue and failures in Ag@Si joints. As the stress distribution tends to stabilize with thermal cycles, the simulation environment was established after five cycles of thermal cycling (−50–250 °C, see Fig. 13a), The detailed modeling of Ag@Si10% and Ag@Si20% joined layers is shown in Fig. 13b. To better reflect the Ag@Si network, the shapes and distribution of Si particles within the joined layers were determined based on the actual SEM cross-section images (refer to Figs. 7a and 8a).

Fig. 14a shows the FEM modeling corresponding to the SiC/DBC die-attached structures. The inset shows the simulation analysis of the joint

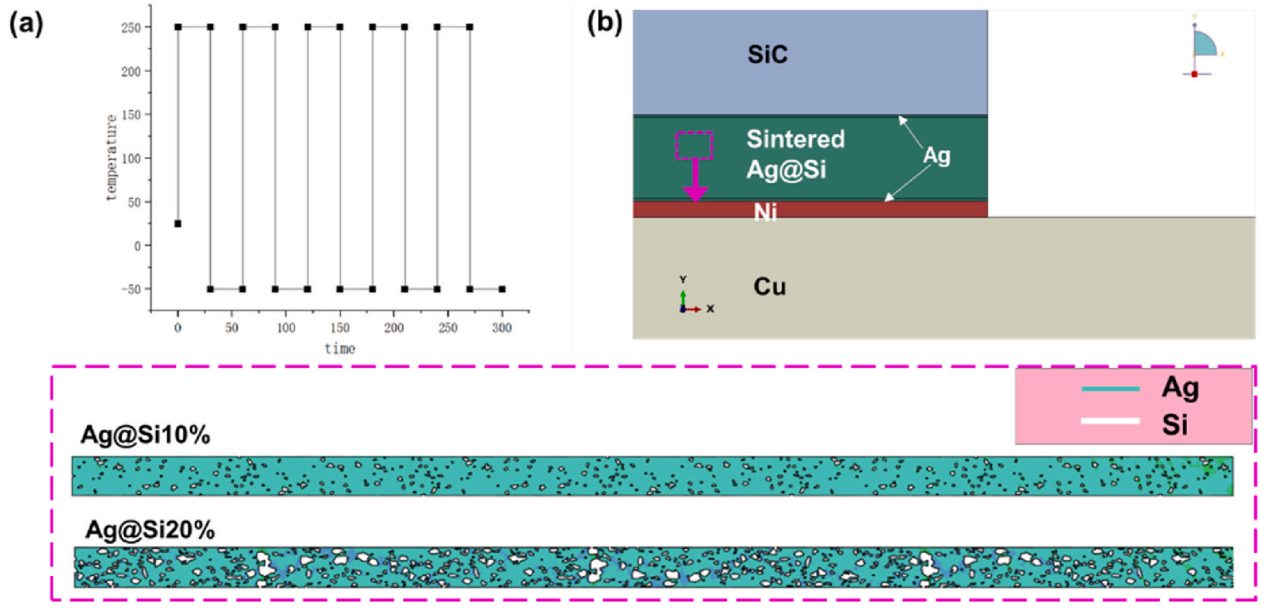

Fig. 13. (a) The FEM simulation condition was under thermal cycling from −50 °C to 250 °C for 5 cycles. (b) The FE modeling of Ag@Si joint structures with magnified Ag@Si10% and Ag@Si20% joined layer. Inset: The distribution and shape of Si additive particles within Ag@Si layers in the model were established based on actual SEM observation.

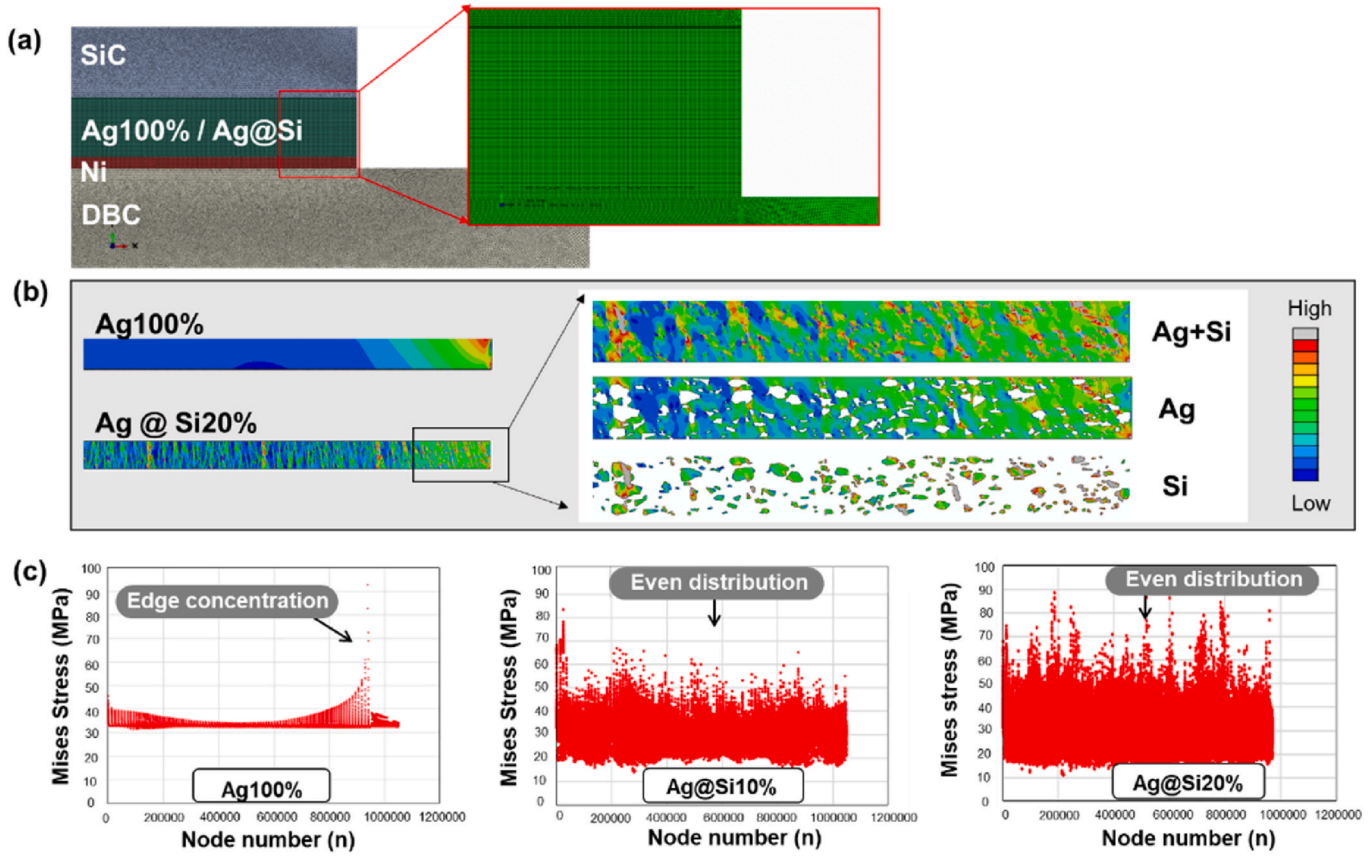

Fig. 14. (a) The Finite-element model corresponding to the die-attached structure consisting of SiC chip, Ag sinter-based paste and EN-ELNPA metallized DBC substrate. (b) In the case of Ag@Si treated as a heterogeneous material, Mises stress distribution in Ag100% and Ag@Si20% joined layers after thermal cycling test. (c) The corresponding stress intensity across nodes within the Ag100%, Ag@Si10% and Ag@Si20% joint structures.

Table 2
The material properties incorporated into the FEM analysis.

PROPERTIES		SiC	Si	Ni	Cu	Si_3N_4
Young's modulus (GPa)		430.00	112.40	163.00	110.00	290.00
Poisson's ratio		0.16	0.28	0.32	0.34	0.27
CTE (ppm/°C)		4.40	3.60	12.49	16.50	2.90
Stress-Plastic strain	**Yielding stress**	/	/	59.00	33.30	/
	Hardness modulus	/	/	16300.00	883.50	/

edge region, as stresses are easily accumulated at the edge of a module structure. In particular, the Mises-stress simulation for the Ag@Si sinter structures was performed from two perspectives to provide comprehensive information, i.e., considering Ag@Si as both a heterogeneous and homogeneous material. In the case of heterogeneous material, the properties of Ag and Si were separately integrated into the FEM, wherein the Ag characteristics was determined according to the above-mentioned thermal and tensile analyses of Ag100% sintered material. In terms of Ag@Si as a homogeneous material, as-obtained tensile properties and CTE of Ag@Si sinter pastes were utilized as composite parameters and applied in the FEM modeling. The properties of the other components are listed in Table II. Among these, the sintered Ag-based pastes, Ni, and Cu were assumed as elasto-plastic materials.

First, in the case of the heterogeneous Ag@Si material, Fig. 14b highlights the Mises-stress distribution in the Ag100% and Ag@Si joined layers, with Ag@Si20% used as the representative case. The distribution of nonuniform stress was observed in the Ag100% layer, wherein the stress was highly concentrated at the joint edge area. While the edge-concentrated stress was effectively alleviated in the Ag@Si20% joined layer; however, numerous high-stress points were dispersed along the bonding layer. When decomposing the stress distribution map of Ag@Si20% layer according to the element, as shown in the magnified view, the stress concentration points were observed to primarily originate from the Ag/Si interfaces; this could be attributed to the stress caused by the Ag/Si–CTE mismatch. As shown in Fig. 14c, the node stress intensity plotting further corroborates the different stress distribution trends caused by the addition of Si. Although all the three joints show a similar maximum stress of ~90 MPa, compared to the dense high-stress nodes at edge in the Ag100% joint, the high-stress nodes are evenly distributed across the Ag@Si joined layers. In this aspect, while the strength of stress was not decreased, the stress distribution within the Ag@Si bonding layer has been uniformized. The achievement of uniform stress distribution in pure sinter Ag joints is of great importance as well, as edge-concentrated stress is highly prone to crack initiation and even the warping of the joint structure [60–62]. The uniform stress distribution allows for elevated joint structure stability, as evidenced by shrinking cracks in the Ag@Si10% joint and the elevated mechanical/-structural reliability in the Ag@Si20% joint.

Furthermore, the Mises-stress distribution and corresponding node stress intensity of the homogeneous Ag@Si material are displayed in Fig. 15. In this case, the three joints show a consistent trend of edge-concentrated stress distribution (See Fig. 15a-c), but there is a noticeable reduction in stress intensity. Fig. 15d shows that most high-stress nodes lie in the intensity level range of 40–60 MPa in the Ag100% joint, with a maximum stress of up to 92 MPa. The addition of 10% Si results in almost no change in stress intensity, while the inclusion of 20% Si demonstrated a decrease in the maximum node stress to 75 MPa, as shown in Fig. 15e and f. By utilizing the Ag@Si20% joined material with reduced CTE to 11.08 ppm/K, we demonstrated that the closer CTE-

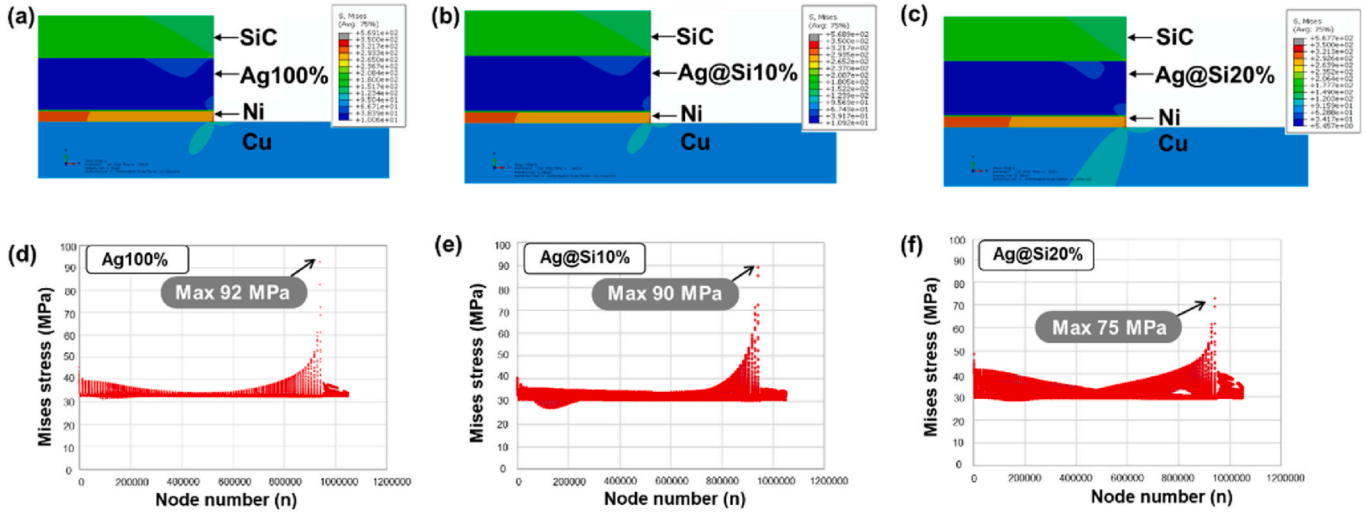

Fig. 15. In the case of Ag@Si treated as a homogeneous material, (a–c) Mises stress distribution in the Ag100%, Ag@Si10% and Ag@Si20% sintering joints. (d–f) The Mises stress intensity across nodes within each joint structure.

matched joint structure experienced less stress build-up and consequently elevated the bonding stability/reliability during thermal cycling. Therefore, from both viewpoints, the Si addition can either favorably even or minimize the Mises stress of the sintered Ag joint structure.

6. Conclusions

This study has successfully sintered micron Ag and Si particles into an integrated network under the low-temperature and pressure-less conditions. The well-bonded Ag@Si sinter matrix allows for inherently good material strength, resulting in high mechanical/microstructural reliability of the die-attached structure under harsh thermal cycles. This is essential for applications, such as electronic components and automotive parts, wherein a consistent performance is required. This novel Ag@Si joined material, with its good cost-effectiveness and superior reliability to that of pure sintered Ag joints, holds significant promise for large-scale, high-power module joining applications.

The key findings of this study are as follows.

(1) With an increase in the Si additive amount, a noticeable inhibitory effect was exhibited on the deterioration of Ag sintered joint during the thermal cycling. That is, the average crack width was obviously narrowed, and the substrate cracking and interface delamination were completely suppressed.
(2) These microstructural improvements ultimately endow the Ag@Si20% joint with much higher mechanical reliability, exhibiting a shear-strength-retention rate twice that of a pure Ag joint.
(3) The effectiveness of mitigated thermo-mechanical stress was collectively demonstrated through CTE measurement, tensile testing, and FEM simulations. In particular, the FEM results showed that Si addition actively adjusted the thermal stress to be uniform or reduced within the module. These factors together contribute to the enhancement of material resistance to thermal cycling stress.

CRediT authorship contribution statement

Yang Liu: Writing – review & editing, Writing – original draft, Formal analysis, Data curation, Conceptualization. **Chuantong Chen:** Writing – review & editing, Supervision, Project administration, Methodology, Investigation, Funding acquisition. **Ye Wang:** Methodology, Investigation, Data curation. **Zheng Zhang:** Validation, Methodology, Investigation, Formal analysis. **Ran Liu:** Formal analysis, Data curation. **Minoru Ueshima:** Methodology, Conceptualization. **Ichiro Ota:** Project administration, Methodology, Investigation. **Hiroshi Nishikawa:** Visualization, Supervision. **Masahiko Nishijima:** Resources, Investigation, Formal analysis. **Koji S. Nakayama:** Methodology, Investigation, Data curation. **Katsuaki Suganuma:** Writing – review & editing, Validation, Supervision.

Declaration of competing interest

The authors declare that they have no known competing financial interests or personal relationships that could have appeared to influence the work reported in this paper.

Data availability

Data will be made available on request.

Acknowledgements

This work was supported by a project (JPNP14004, Grant Number 21502156–0) commissioned by the New Energy and Industrial Technology Development Organization (NEDO) and JSPS KAKENHI (Grant Number 22K04243), and JST (Grant number JPMJSF23DB). The author acknowledges both of financial support and material supply from Daicel Corporation and Murata Science Foundation.

Appendix A. Supplementary data

Supplementary data to this article can be found online at https://doi.org/10.1016/j.compositesb.2024.111519.

References

[1] Reese SB, Remo T, Green J, Zakutayev A. How much will gallium oxide power electronics cost? Joule 2019;3(4):903–7.
[2] Lumbreras D, Zaragoza J, Berbel N, Mon J, Gálvez E, Collado A. Comprehensive analysis of hexagonal sigma-delta modulations for three-phase high-frequency VSC based on wide-bandgap semiconductors. IEEE Trans Power Electron 2020;36(6):7212–22.
[3] Zhao S, Chen C, Haga M, Ueshima M, Hirahara H, Sang J, hun Cho S, Sekino T, Suganuma K. Failure mechanisms of the bonded interface between mold epoxy and metal substrate exposed to high temperature. Compos B Eng 2023;254:110562.

[4] Tatsumi H, Nishikawa H. Anisotropic highly conductive joints utilizing Cu-solder microcomposite structure for high-temperature electronics packaging. Mater Des 2022;223:111204.
[5] Guo L, Liu W, Ji X, Zhong Y, Hang C, Wang C. Robust Cu–Cu bonding with multiscale coralloid nano-Cu3Sn paste for high-power electronics packaging. ACS Appl Electron Mater 2022;4(7):3457–69.
[6] Yuan L, Xiong J, Ren J, Yang T, Xiao X, Ma Y, Luan J, Li J. Ultrastrong and ductile transient liquid phase (TLP) bonding joints reinforced by ordered multi-precipitates. Compos B Eng 2022;231:109568.
[7] Choi EB, Lee Y-J, Lee J-H. Rapid sintering by thermo-compression in air using a paste containing bimodal-sized silver-coated copper particles and effects of particle size and surface finish type. J Alloys Compd 2022;897:163223.
[8] Lee CH, Choi EB, Lee J-H. Characterization of novel high-speed die attachment method at 225° C using submicrometer Ag-coated Cu particles. Scripta Mater 2018; 150:7–12.
[9] Kim MI, Lee J-H. Die sinter bonding in air using Cu@ Ag particulate preform and rapid formation of near-full density bondline. J Mater Res Technol 2021;14: 1724–38.
[10] Yuan Y, Wu H, Li J, Zhu P, Sun R. Cu-Cu joint formation by low-temperature sintering of self-reducible Cu nanoparticle paste under ambient condition. Appl Surf Sci 2021;570:151220.
[11] Yang G, Wang P, Liu Y, Lu S, Luo B, Lai T, Ta S, Lin T, Luo J, Zhang Y. Effect of Ag coating on the oxidation resistance, sintering properties, and migration resistance of Cu particles. J Alloys Compd 2022;923:166271.
[12] Li Y, Xu L, Jing H, Zhao L, Hao K, Han Y. Study on the floating kinetics of graphene in molten Sn-based alloy based on in-situ observation of X-ray radiography. Compos B Eng 2022;238:109909.
[13] Peng P, Hu A, Gerlich AP, Zou G, Liu L, Zhou YN. Joining of silver nanomaterials at low temperatures: processes, properties, and applications. ACS Appl Mater Interfaces 2015;7(23):12597–618.
[14] Yu F, Cui J, Zhou Z, Fang K, Johnson RW, Hamilton MC. Reliability of Ag sintering for power semiconductor die attach in high-temperature applications. IEEE Trans Power Electron 2016;32(9):7083–95.
[15] Zabihzadeh S, Van Petegem S, Holler M, Diaz A, Duarte L, Van Swygenhoven H. Deformation behavior of nanoporous polycrystalline silver. Part I: microstructure and mechanical properties. Acta Mater 2017;131:467–74.
[16] Ding C, Liu H, Ngo KD, Burgos R, Lu G-Q. A double-side cooled SiC MOSFET power module with sintered-silver interposers: I-design, simulation, fabrication, and performance characterization. IEEE Trans Power Electron 2021;36(10):11672–80.
[17] Li J, Li X, Wang L, Mei Y-H, Lu G-Q. A novel multiscale silver paste for die bonding on bare copper by low-temperature pressure-free sintering in air. Mater Des 2018; 140:64–72.
[18] Chen TF, Siow KS. Comparing the mechanical and thermal-electrical properties of sintered copper (Cu) and sintered silver (Ag) joints. J Alloys Compd 2021;866: 158783.
[19] Kim D, Nagao S, Chen C, Wakasugi N, Yamamoto Y, Suetake A, Takemasa T, Sugahara T, Suganuma K. Online thermal resistance and reliability characteristic monitoring of power modules with Ag sinter joining and Pb, Pb-free solders during power cycling test by SiC TEG chip. IEEE Trans Power Electron 2020;36(5): 4977–90.
[20] Chen C, Nagao S, Suganuma K, Jiu J, Sugahara T, Zhang H, Iwashige T, Sugiura K, Tsuruta K. Macroscale and microscale fracture toughness of microporous sintered Ag for applications in power electronic devices. Acta Mater 2017;129:41–51.
[21] Huo F, Jin Z, Le Han D, Li J, Zhang K, Nishikawa H. Novel interface regulation of Sn1. 0Ag0. 5Cu composite solders reinforced with modified ZrO2: microstructure and mechanical properties. J Mater Sci Technol 2022;125:157–70.
[22] Jia Q, Zou G, Wang W, Ren H, Zhang H, Deng Z, Feng B, Liu L. Sintering mechanism of a supersaturated Ag–Cu nanoalloy film for power electronic packaging. ACS Appl Mater Interfaces 2020;12(14):16743–52.
[23] Yang F, Zhu W, Wu W, Ji H, Hang C, Li M. Microstructural evolution and degradation mechanism of SiC–Cu chip attachment using sintered nano-Ag paste during high-temperature ageing. J Alloys Compd 2020;846:156442.
[24] Yan J. A review of sintering-bonding technology using Ag nanoparticles for electronic packaging. Nanomaterials 2021;11(4):927.
[25] Chen C, Zhao S, Sekiguchi T, Suganuma K. Large-scale bare Cu bonding by 10 μm-sized Cu–Ag composite paste in low temperature low pressure air conditions. J Sci: Advanced Materials and Devices 2023;8(3):100606.
[26] Kim D, Kim M-S. Macroscale and microscale structural mechanisms capable of delaying the fracture of low-temperature and rapid pressureless Ag sintered electronics packaging. Mater Char 2023;198:112758.
[27] Huang WC, Tsai CH, Lee PT, Kao C. Effects of bonding pressures on microstructure and mechanical properties of silver–tin alloy powders synthesized by ball milling for high-power electronics packaging. J Mater Res Technol 2022;19:3828–41.
[28] Bhogaraju SK, Conti F, Kotadia HR, Keim S, Tetzlaff U, Elger G. Novel approach to copper sintering using surface enhanced brass micro flakes for microelectronics packaging. J Alloys Compd 2020;844:156043.
[29] Gao Y, Li W, Chen C, Zhang H, Jiu J, Li C-F, Nagao S, Suganuma K. Novel copper particle paste with self-reduction and self-protection characteristics for die attachment of power semiconductor under a nitrogen atmosphere. Mater Des 2018; 160:1265–72.
[30] Zhang S, Wang Q, Lin T, Zhang P, He P, Paik K-W. Cu-Cu joining using citrate coated ultra-small nano-silver pastes. J Manuf Process 2021;62:546–54.
[31] Su Y, Fu G, Liu C, Liu C, Long X. Fatigue crack evolution and effect analysis of Ag sintering die-attachment in SiC power devices under power cycling based on phase-field simulation. Microelectron Reliab 2021;126:114244.
[32] Ren H, Zou G, Jia Q, Deng Z, Du C, Wang W, Liu L. Thermal stress reduction strategy for high-temperature power electronics with Ag sintering. Microelectron Reliab 2021;127:114379.
[33] Zhang B, Zhang S, Lu X, Han L, Mei Y-H. Reliability improvement of low-temperature sintered nano-silver as die attachment by porosity optimization. IEEE Trans Compon Packag Manuf Technol 2023.
[34] Yi H, Mei S, Shen H, Zhang R, Li Z. Enhancing thermal mechanical properties of polymer composites with hollow porous fillers. Compos Appl Sci Manuf 2024;179: 108048.
[35] Guo Q, Li G, Zhu P, Xu Z, Zhao T, Sun R, Wong C-p. Interfacial engineering of epoxy/silica nanocomposites by amino-rich polyethyleneimine towards simultaneously enhanced rheological and thermal-mechanical performance for electronic packaging application. Compos B Eng 2022;245:110214.
[36] Cheng Y-T, Lin K-L, Lin C-C. Preparing Silver–Copper pastes in accordance with percolation theory for die attach bonding. Mater Chem Phys 2023;297:127391.
[37] Tan KS, Wong YH, Cheong KY. Thermal characteristic of sintered Ag–Cu nanopaste for high-temperature die-attach application. Int J Therm Sci 2015;87:169–77.
[38] Yin C, Wumaeraili K, Zhang Y, Wu Y, Zhang J, Guo W, Zhu Y, Song X, Jia Q, Zhang H. Novel Ag-Cu foam sheet with multi-layer composite structure for high performance joining of SiC power chips. Mater Char 2024;209:113696.
[39] Liu L, Shi R, Zhang S, Liu W, Huang S, Chen Z. Effects of Ag shell on electrical, thermal and mechanical properties of Cu@ Ag composite solder preforms by electromagnetic compaction for power electronics. Mater Char 2023;197:112702.
[40] Zhang H, He S, Qu G, Deng Z, Zou G, Jia Q, Deng E, Guo W. Improved thermal conductivity and reliability through graphene reinforced nanopaste for power devices in new energy vehicles. IEEE Trans Compon Packag Manuf Technol 2023.
[41] Long X, Li Z, Lu X, Guo H, Chang C, Zhang Q, Zehri A, Ke W, Yao Y, Ye L. Mechanical behaviour of sintered silver nanoparticles reinforced by SiC microparticles. Materials Science and Engineering: A 2019;744:406–14.
[42] Chen C, Suganuma K. Microstructure and mechanical properties of sintered Ag particles with flake and spherical shape from nano to micro size. Mater Des 2019; 162:311–21.
[43] Kim D, Chen C, Nagao S, Suganuma K. Mechanical characteristics and fracture behavior of GaN/DBA die-attached during thermal aging: pressure-less hybrid Ag sinter joint and Pb–5Sn solder joint. J Mater Sci Mater Electron 2020;31:587–98.
[44] Fan T, Zhang H, Shang P, Li C, Chen C, Wang J, Liu Z, Suganuma K. Effect of electroplated Au layer on bonding performance of Ag pastes. J Alloys Compd 2018; 731:1280–7.
[45] Chen C, Kim D, Zhang Z, Wakasugi N, Liu Y, Hsieh M-C, Zhao S, Suetake A, Suganuma K. Interface-mechanical and thermal characteristics of Ag sinter joining on bare DBA substrate during aging, thermal shock and 1200 W/cm 2 power cycling tests. IEEE Trans Power Electron 2022;37(6):6647–59.
[46] Arsha A, Manoj V, Akhil M, Anbukkarasi R, Rajimol P, Rajan T. Squeeze infiltration processing and characterization of silicon reinforced composites. Mater Today Commun 2022;32:103870.
[47] Adhitama E, Dias Brandao F, Dienwiebel I, Bela MM, Javed A, Haneke L, Stan MC, Winter M, Gomez-Martin A, Placke T. Pre-lithiation of silicon anodes by thermal evaporation of lithium for boosting the energy density of lithium ion cells. Adv Funct Mater 2022;32(22):2201455.
[48] Coppola L, Huff D, Wang F, Burgos R, Boroyevich D. Survey on high-temperature packaging materials for SiC-based power electronics modules. 2007 IEEE power electronics specialists conference. IEEE; 2007. p. 2234–40.
[49] Liu Y, Chen C, Zhang Z, Ueshima M, Sakamoto T, Naoe T, Nishikawa H, Oda Y, Suganuma K. Development of crack-less and deformation-resistant electroplated Ni/electroless Ni/Pt/Ag metallization layers for Ag-sintered joint during a harsh thermal shock. Mater Des 2022;224:111389.
[50] Zhang L, Li P, Li S, Nie F, Wu B, Li C, Li J, Zhang Z, Jiang X, Zhao B. Superior shear strength subject to the regulation of plastic toughness in K4169 alloy/TiAl intermetallic joints vacuum brazed with gradient composite amorphous filler metals. Compos B Eng 2024:111288.
[51] Park B-G, Myung W-R, Lee C-J, Jung S-B. Mechanical, electrical, and thermal reliability of Sn-58wt.% Bi solder joints with Ag-decorated MWCNT for LED package component during aging treatment. Compos B Eng 2020;182:107617.
[52] Zhang Z, Chen C, Suetake A, Hsieh M-C, Iwaki A, Suganuma K. Pressureless and low-temperature sinter-joining on bare Si, SiC and GaN by a Ag flake paste. Scripta Mater 2021;198:113833.
[53] Manikam VR, Razak KA, Cheong KY. Sintering of silver–aluminum nanopaste with varying aluminum weight percent for use as a high-temperature die-attach material. IEEE Trans Compon Packag Manuf Technol 2012;2(12):1940–8.
[54] Heuck N, Langer A, Stranz A, Palm G, Sittig R, Bakin A, Waag A. Analysis and modeling of thermomechanically improved silver-sintered die-attach layers modified by additives. IEEE Trans Compon Packag Manuf Technol 2011;1(11): 1846–55.
[55] Xu Y, Qiu X, Li W, Wang S, Ma N, Ueshima M, Chen C, Suganuma K. Development of high thermal conductivity of Ag/diamond composite sintering paste and its thermal shock reliability evaluation in SiC power modules. J Mater Res Technol 2023;26:1079–93.
[56] Wang M, Mei Y, Hu W, Li X, Lu G-Q. Pressureless sintered-silver as die attachment for bonding Si and SiC chips on silver, gold, copper, and nickel metallization for power electronics packaging: the practice and science. IEEE Journal of Emerging and Selected Topics in Power Electronics 2022;10(2):2645–55.
[57] Kim D, Chen C, Lee S, Kim M-S, Suganuma K. Controlling the thermal aging and Kirkendall void diffusion speed of sputtered silver interlayers in GaN power semiconductor packaging interfaces for in-wheel motor system integrations. Corrosion Sci 2024;226:111614.

[58] Watanabe T, Takesue M, Matsuda T, Sano T, Hirose A. Thermal stability and characteristic properties of pressureless sintered Ag layers formed with Ag nanoparticles for power device applications. J Mater Sci Mater Electron 2020;31:17173–82.
[59] Venkataraman A, Linne M, Daly S, Sangid MD. Criteria for the prevalence of grain boundary sliding as a deformation mechanism. Materialia 2019;8:100499.
[60] Chen C, Nagao S, Zhang H, Jiu J, Sugahara T, Suganuma K, Iwashige T, Sugiura K, Tsuruta K. Mechanical deformation of sintered porous Ag die attach at high temperature and its size effect for wide-bandgap power device design. J Electron Mater 2017;46:1576–86.
[61] Dudek R, Sommer P, Fix A, Trodler J, Rzepka S, Michel B. Reliability investigations for high temperature interconnects. Solder Surf Mt Technol 2014;26(1):27–36.
[62] Siow K, Chua S. Thermal cycling of sintered silver (Ag) joint as die-attach material. JOM 2019;71(9):3066–75.